Journal of Materials Chemistry A

ROYAL SOCIETY OF CHEMISTRY

PAPER

View Article Online
View Journal | View Issue

Cite this: J. Mater. Chem. A, 2023, 11, 15319

Facile synthesis of cobalt fluoride (CoF_2)/multi-walled carbon nanotube (MWCNT) nanocomposites and improvement of their electrochemical performance as cathode materials for Li-ion batteries†

Hayoung Park, [ab] Il-Seop Jang, [ab] Bo-Ye Song, [ab] Yun Chan Kang, [b] Seongseop Kim *[c] and Jinyoung Chun *[a]

Conversion-type metal fluoride cathodes are considered promising candidates for electrochemical applications owing to their large specific capacities and high operating voltages. However, harnessing the potentially high energy-density of metal fluorides is challenging because of their inherent chemical and electrochemical properties and synthesis issues. Cobalt fluoride (CoF_2) is an attractive cathode material among metal fluorides, but it has the common limitations of metal fluorides as above. In this study, a facile synthesis method for CoF_2 nanocomposites is developed through the precipitation of cobalt precursors onto multi-walled carbon nanotubes (MWCNTs), followed by heat treatment with ammonium fluoride under an inert atmosphere. This simple and versatile method produces CoF_2/MWCNT nanocomposites with improved reversible capacities (554 mA h g^{-1} at 0.2C) through conversion reactions and superior rate capabilities (a capacity retention of 84.7% at 2C *versus* 0.2C) at high current densities. In addition, to prevent capacity fading caused by cobalt dissolution during battery cycling, further *in situ* and *ex situ* strategies for surface protection are adopted: *in situ* formation of cathode–electrolyte interphase layers using a fluoroethylene carbonate-containing electrolyte and *ex situ* coating of aluminum oxide thin layers on the electrode by atomic layer deposition. Consequently, the CoF_2/MWCNT nanocomposites maintain a capacity of more than 200 mA h g^{-1} even after 500 cycles. This study is expected to promote the development of advanced metal fluoride cathodes with high energy densities and long cycle lives.

Received 31st March 2023
Accepted 14th June 2023

DOI: 10.1039/d3ta01918g

rsc.li/materials-a

[a]*Emerging Materials R&D Division, Korea Institute of Ceramic Engineering and Technology (KICET), Jinju 52851, Republic of Korea. E-mail: jchun@kicet.re.kr*

[b]*Department of Materials Science and Engineering, Korea University, Seoul 02841, Republic of Korea*

[c]*School of Chemical Engineering, Clean Energy Research Center, Jeonbuk National University, Jeonju 54896, Republic of Korea. E-mail: seongseopkim@jbnu.ac.kr*

† Electronic supplementary information (ESI) available. See DOI: https://doi.org/10.1039/d3ta01918g

Dr Seongseop Kim is an assistant professor in the School of Chemical Engineering at Jeonbuk National University (JBNU). He received his B.S. degree in Chemical Engineering from Hanyang University (2013), and PhD degree in Chemical Engineering from POSTECH (2019). During the PhD course, he joined Rensselaer Polytechnic Institute as a visiting student. After his PhD, he worked as a postdoctoral research at KAIST and Max Planck Institute für Kohlenforschung. His research interests focus on the design of nano- and meso-porous inorganic materials for electrocatalysis and energy applications.

Introduction

Cathode materials for Li-ion batteries (LIBs) with high energy-densities are essential to meet the increased energy consumption of portable devices, rapid growth of the electric vehicle industry, and increasing demand for advanced energy storage systems. Intercalation-based high-Ni cathode materials, such as $LiNi_{0.8}Co_{0.15}Al_{0.05}O_2$ (NCA) and $LiNi_{0.8}Co_{0.1}Mn_{0.1}O_2$ (NCM811), have attracted significant attention because of their improved energy densities due to the increased availability of lithium ions.[1–3] However, the number of lithium ions available per unit molecule of active material is still limited, having a theoretical capacity of approximately 250 mA h g^{-1}, thus restricting the achievement of the energy density required by modern industry. Therefore, to solve the intrinsic capacity limitation issues of lithium-ion intercalation materials, researchers have focused on new electrode materials that react with lithium ions through conversion or alloying reactions, which can take up multiple lithium ions per unit formula.[4–9]

Among the metal compounds that undergo conversion reactions, such as metal oxides, nitrides, sulfides, and fluorides, metal fluorides (MF_x) are a promising cathode candidate for LIBs.[10–17] MF_x exhibit high operating voltages because of the strong ionic characteristics of the M–F bond,[10] as well as large gravimetric and volumetric specific capacities, as 2–3 lithium ions can be stored per transition metal atom (redox center, *e.g.*, Fe, Ni, Cu, and Co) in MF_x cathodes.[11] However, utilizing the potentially high energy density of MF_x has been a challenge over the last several decades owing to their synthesis difficulties and inherent chemical and electrochemical properties.[12–14,18]

Cobalt fluoride (CoF_2), a member of the MF_x family, provides high theoretical specific capacities (553 mA h g^{-1} and 2038 mA h cm^{-3}) that relate to a two-electron transfer per formula unit of CoF_2 and promising energy densities (828 W h kg^{-1} and 1565 W h L^{-1}) in CoF_2–Li batteries (Fig. S1†).[19,20] However, CoF_2 also has the common drawbacks of MF_x cathode materials: (i) limited synthesis and nanostructuring methods, (ii) low electronic conductivities originating from high-ionic bonding characteristics and a large bandgap (4.44 eV), (iii) large voltage hysteresis caused by conversion reactions, and (iv) dissolution of metal ions at high voltages.

Among these challenges, the low electronic conductivity and poor kinetics of bulk-sized materials are critical drawbacks of using CoF_2 as a cathode for LIBs. Hence, the introduction of nanostructures and the formation of composites with conducting agents are essential preconditions for the application of CoF_2 as a cathode material. However, the synthesis methods developed in previous studies have several disadvantages, such as complicated manufacturing processes,[21] expensive precursors,[21,22] and the need for heat treatment facilities to handle high-risk fluorine-based gases.[23] In several studies, the relatively large particle size of CoF_2 resulted in poor electrochemical performance.[24–26] Although the preparation of designed CoF_2 nanocomposites incorporated in conducting carbons and respective improved electrochemical properties have been reported recently,[23,27,28] a large portion of inactive carbon components (approximately 40 wt% or more) and the requirement of complex synthetic processes are challenges remaining to be addressed. In addition, the rapid dissolution of transition metal cations at high voltages is observed during the conversion reactions of CoF_2. This phenomenon significantly reduces the reversibility of reactions and cause fatal side reactions within the cell, thus hindering the long cycle life of batteries.[23,29] Therefore, to improve the cycle performance of MF_x, electrolyte optimization and surface modification of the electrodes to prevent the dissolution of active materials should be conducted simultaneously.

In this study, a facile synthesis method for CoF_2 nanocomposites was developed and additional *in situ* and *ex situ* surface protection strategies were introduced to improve their electrochemical performance. CoF_2/multi-walled carbon nanotube (MWCNT) nanocomposites were prepared by simple precipitation of cobalt precursors onto MWCNTs, followed by heat treatment with ammonium fluoride (NH_4F). During this synthesis process, special facilities for high-pressure solvothermal reactions and handling of toxic gases are not necessary. Consequently, the synthesis procedure is not only simple and versatile but also relatively safe. Compared with the CoF_2 particles obtained in the absence of MWCNTs, CoF_2/MWCNTs exhibited improved specific capacities through conversion reactions and superior rate capabilities at high current densities. In addition, the *in situ* formation of a cathode electrolyte interphase (CEI) layer using a fluoroethylene carbonate (FEC)-containing electrolyte and *ex situ* coating of an aluminium oxide (Al_2O_3) thin layer on the electrode by atomic layer deposition (ALD) effectively mitigated rapid capacity decay originating from metal ion dissolution. This study contributes to the development of advanced MF_x cathodes based on conversion reactions for high-energy-density batteries with long cycle lives.

Experimental section

Synthesis of CoF_2/MWCNT nanocomposites

$Co(NO_3)_2 \cdot 6H_2O$ (97.0%, Junsei Chemical), NH_4HCO_3 (95.0%, Junsei Chemical), and NH_4F (97.0%, Junsei Chemical) were used as received, without further purification. MWCNTs (MR99, Carbon Nano-material Technology Co., Ltd) were used after acid treatment by following a previously reported procedure.[30] Cobalt precursor–MWCNT nanocomposites were obtained using a precipitation method. $Co(NO_3)_2 \cdot 6H_2O$ ethanolic solution (5 mmol) was prepared, and MWCNTs were added, at a mass ratio of CoF_2 : MWCNTs of 7 : 3. MWCNTs were dispersed by ultrasonication. Subsequently, NH_4HCO_3 was dissolved in the solution and stirred for 12 h to form the cobalt precursor. The products were washed with deionized water to remove impurities and dried at 80 °C in a vacuum oven. The resultant powder was mechanically ground with NH_4F at a mass ratio of 1 : 1 using a mortar and pestle. The mixture was heat treated at 250 °C for 2 h under a nitrogen atmosphere to prevent oxidation. The final product was denoted as CoF_2/MWCNTs. For comparison, CoF_2 particles were synthesized using only cobalt precursors and NH_4F in the absence of MWCNTs and denoted as bare-CoF_2.

Al_2O_3 coatings onto the electrodes through atomic layer deposition (ALD)

Al_2O_3 coating on the CoF_2/MWCNT electrode was carried out at 120 °C with a growth rate of 0.1 nm per cycle using an ALD system (Lucida D100, NCD). Trimethylaluminum (TMA, $Al(CH_3)_3$) and H_2O were used as the precursors and a complete ALD cycle included: (1) pulsing TMA for 0.2 s, (2) purging the chamber for 10 s, (3) pulsing H_2O for 0.2 s, and (4) purging the chamber for 10 s. The CoF_2/MWCNT electrodes were coated with Al_2O_3 through 20 or 50 ALD cycles, and named 20A- and 50A-CoF_2/MWCNTs, respectively.

Materials characterization

The crystal structure of the prepared samples was obtained by powder X-ray diffraction (XRD; D8 Advance, Bruker) using Cu Kα radiation ($\lambda = 1.5418$ Å) in the diffraction angle (2θ) range of 10–80°. The morphologies were observed using field-emission scanning electron microscopy (FE-SEM; JSM-7610F, JEOL) at a working voltage of 10.0 kV, and field-emission transmission electron microscopy (FE-TEM; JEM-4010, JEOL) at a working voltage of 300 kV. The elemental mapping results were investigated by FE-TEM (Tecnai G2 F30, FEI). The chemical bonding states were analyzed using X-ray photoelectron spectroscopy (XPS; Nexsa, Thermo Fisher Scientific) with Al Kα radiation (1486.6 eV). The XPS depth profile analysis was performed by etching with an Ar ion beam. The MWCNT content was measured by thermogravimetric analysis (TGA; STA7300, Hitachi) under an air atmosphere at a heating rate of 10 °C min^{-1}.

Electrochemical characterization

To prepare the electrode, the active material, conducting carbon (Super P), and polyvinylidene difluoride (PVDF) were mixed in a weight ratio of 8 : 1 : 1 with *N*-methyl-2-pyrrolidone (NMP) using a Thinky mixer (ARE-310, THINKY Co.). The resulting slurries were coated onto aluminum foils using the doctor-blade method. The electrode was dried in a vacuum oven at 80 °C overnight and punched into 12-pi circular discs for use as the working electrode. Coin-type cells (CR2032) were assembled in a dry room, in which Li foil was used as the reference and counter electrodes. A polypropylene (PP) film (Celgard 2500) was used as the separator and 1.0 M $LiPF_6$ in ethylene carbonate/dimethyl carbonate (EC/DMC, 1 : 1 volume ratio, Enchem Co.) and 1.0 M $LiPF_6$ in fluoroethylene carbonate/ethyl methyl carbonate (FEC/EMC, 30 : 70 volume ratio, Enchem Co.) were used as the electrolyte. Using a WBCS-3000 battery cycler (WonATech Co.), cyclic voltammetry (CV) and galvanostatic charge/discharge analyses were conducted in the potential range of 1.0 to 4.0 V (*vs.* Li/Li^+). The specific capacities and C-rates were calculated based on the masses of the active materials. The rate of 1C corresponded to a current density of 553 mA g^{-1}. Electrochemical impedance spectroscopy (EIS) measurements were performed using a potentiostat (SP-300, BioLogic) over the frequency range between 0.1 Hz and 1 MHz. For galvanostatic intermittent titration technique (GITT) analysis, a current pulse of 100 mA g^{-1} was applied for 1 h, followed by a relaxation period of 10 h.

Results and discussion

Synthesis of CoF_2/MWCNT nanocomposites and their electrochemical properties

The procedure developed for the synthesis of CoF_2/MWCNTs is shown in Fig. 1. Through the precipitation method using NH_4HCO_3, nano-sized Co precursors were well distributed on the MWCNTs (Fig. S2a and b†). After mechanical grinding with NH_4F and heat treatment, the Co precursor/MWCNTs were easily converted to CoF_2/MWCNT nanocomposites. Through these processes, CoF_2/MWCNTs can be effectively prepared without complicated synthetic procedures or the direct use of hazardous reagents (*e.g.*, fluorine gas and hydrogen fluoride solutions).

The obtained XRD patterns of CoF_2/MWCNTs and bare-CoF_2 are shown in Fig. 2a. All diffraction peaks matched those of

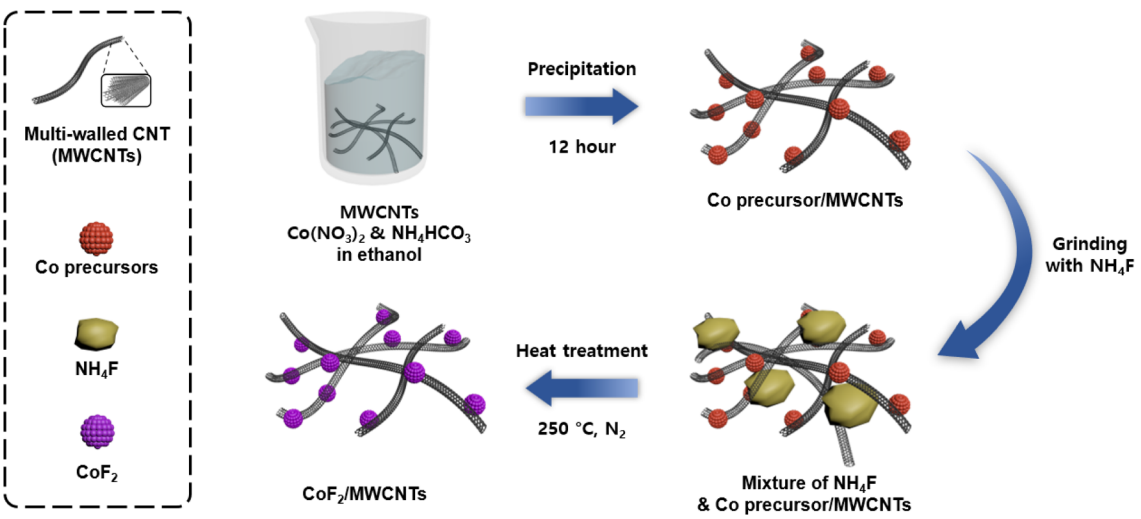

Fig. 1 Schematics of CoF_2/MWCNT nanocomposite synthesis.

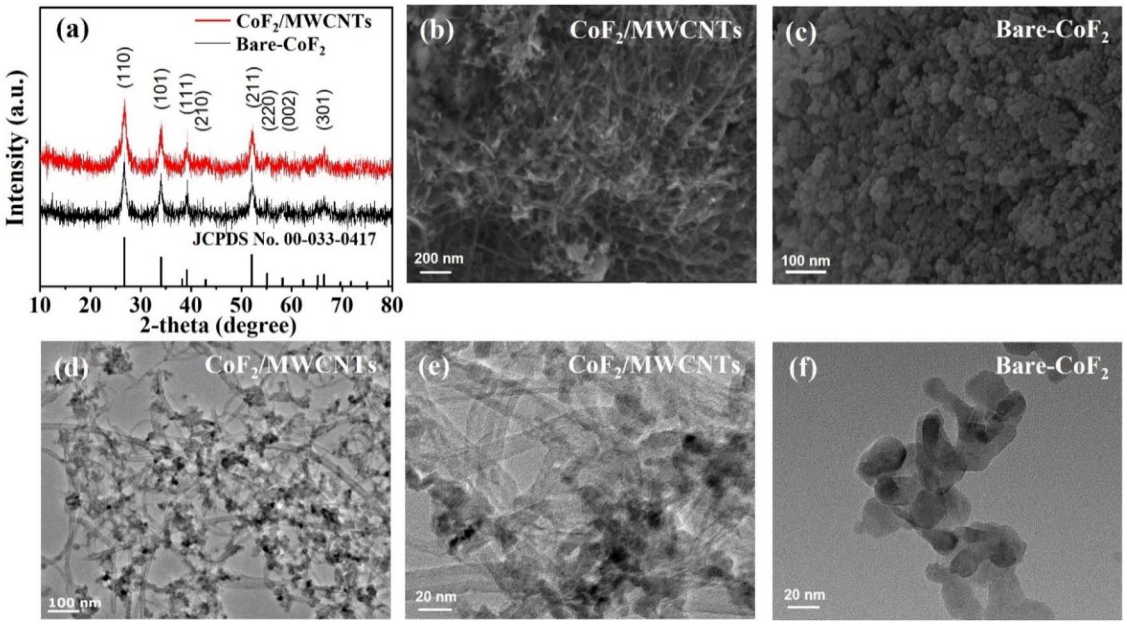

Fig. 2 (a) XRD patterns of CoF_2/MWCNTs and bare-CoF_2. SEM images of (b) CoF_2/MWCNTs and (c) bare-CoF_2. TEM images of (d and e) CoF_2/MWCNTs and (f) bare-CoF_2.

tetragonal CoF_2 (JCPDS No. 00-033-0417) and no other impurity peaks were observed. A small shoulder peak was observed at approximately 26° because of the carbon substrates, which demonstrates the presence of MWCNTs in CoF_2/MWCNTs (Fig. S2c†). The XRD patterns of bare-CoF_2 also presented the same CoF_2 crystal structure without the MWCNT peak. Considering that the XRD peaks of CoF_2/MWCNTs and bare-CoF_2 appeared broad rather than narrow, the crystallite size was assumed to be small. SEM and TEM analyses were performed to confirm the particle size and morphology. In the case of CoF_2/MWCNTs, nano-sized (10–15 nm) CoF_2 particles were spread on the MWCNTs (Fig. 2b, d and e). Compared with Co precursors/MWCNTs (Fig. S2a and b†), the morphology of CoF_2 nanoparticles in CoF_2/MWCNTs was well maintained after heat treatment. By contrast, bare-CoF_2 consisted of randomly aggregated particles composed of 20 nm-sized primary particles (Fig. 2c and f). These results show that the synthetic method used in this study was effective in preparing nanocomposites in which small-sized CoF_2 nanoparticles were well-dispersed on the conductive nanocarbons.

The presence of CoF_2 nanoparticles in the synthesized nanocomposite was further confirmed by elemental mapping of CoF_2/MWCNTs (Fig. 3). The mapping signals confirmed that the nanoparticles on the MWCNTs consisted of cobalt and fluorine. XPS analysis was performed to confirm the composition of the nanocomposites (Fig. 4). The high-resolution Co 2p XPS spectrum exhibited two distinct peaks at 783.9 and 800.0 eV for Co^{2+} $2p_{3/2}$ and Co^{2+} $2p_{1/2}$, respectively (Fig. 4a) and an F 1s peak located at 686.0 eV which are characteristic to CoF_2.[31] Regarding the C 1s spectrum, the peak located at 284.6 eV corresponds to C–C bonding from the MWCNTs. The small peak observed at 286.0 eV is associated with the contribution of C–O functionalities. These functional groups containing oxygen atoms provide nucleation sites for cobalt precursors and prevent excessive particle aggregation.[32,33]

The loading amount of CoF_2 in the CoF_2/MWCNTs was confirmed by TGA (Fig. S3†). CoF_2/MWCNTs were fully converted into Co_3O_4 through heat treatment at 700 °C under an air atmosphere, thus leading to a mass loss of approximately 43%. Considering the mass changes originating from the

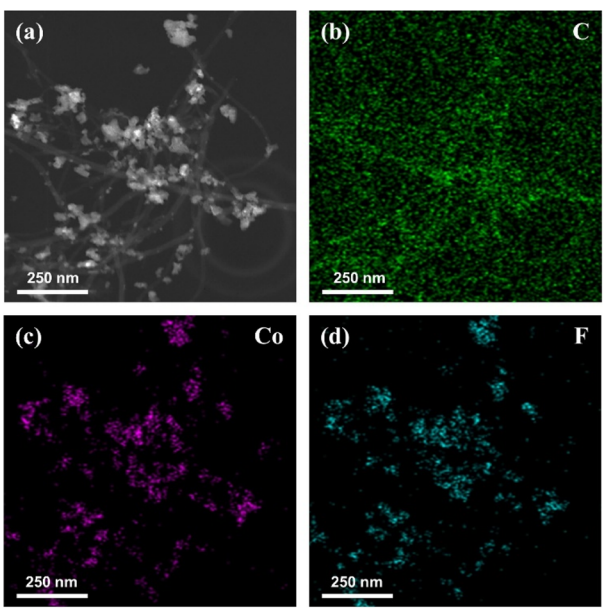

Fig. 3 (a) Scanning transmission electron microscope (STEM) image of CoF_2/MWCNTs. Energy-dispersive X-ray spectroscopy (EDS) elemental mapping of (b) carbon, (c) cobalt, and (d) fluorine.

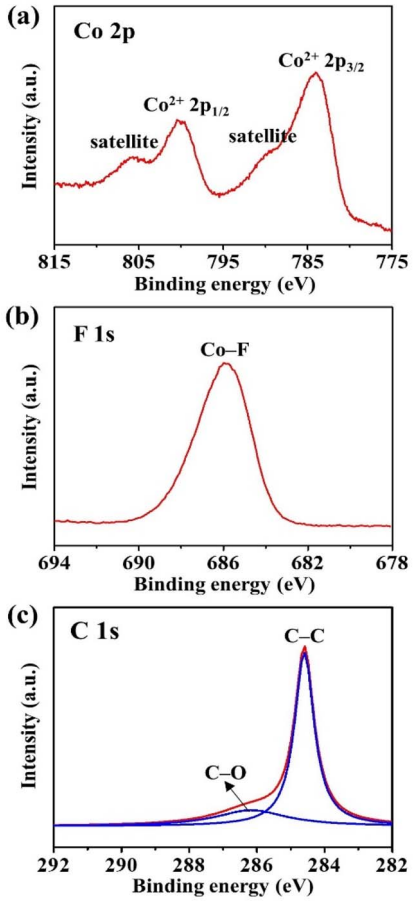

Fig. 4 XPS spectra of CoF_2/MWCNTs: (a) Co 2p, (b) F 1s, and (c) C 1s.

oxidation of CoF_2 to Co_3O_4 and the decomposition of MWCNTs simultaneously, the loading amount of CoF_2 calculated from the TGA results was approximately 68 wt%, which was consistent with the target value (70 wt%). This result indicates that heat treatment with NH_4F in a solventless system is effective for the fluorination of cobalt precursors without product loss.

The electrochemical reactions of CoF_2/MWCNTs were examined using CV tests at a scan rate of 0.1 mV s^{-1} between 1.0 and 4.0 V (*vs.* Li/Li^+) (Fig. 5a). A large intensity reduction peak was observed in the voltage range of approximately 1.12 V, which corresponds to the lithiation of CoF_2 through conversion reactions.[25,34] Next, small anodic peaks appeared at 3.1–3.2 V, and the small cathodic peaks were displayed at 2.0–2.1 V. In contrast to the first reduction peak, a pair of broad anionic and cathodic peaks were observed. The voltage difference between the first reduction and oxidation peaks of CoF_2/MWCNTs was approximately 2.0 V and decreased to 1.1–1.2 V as the battery cycled. These are unique characteristics of the conversion reactions: as CoF_2 converted to Co and LiF, the crystallite sizes of each component significantly decreased.[24,35] Next, reconversion/conversion reactions occurred in these small crystallite sizes; hence, broad anodic/cathodic peaks were observed after the first reduction step, and the redox potential difference decreased. On the other hand, it was observed that the potential difference slightly increased in the 3rd cycle compared to the 2nd cycle. The dissolution of metallic Co during cycling led to the accumulation of insulating LiF, which is detrimental to the electronic and ionic transport in the electrode.[36] Therefore, it is assumed that partial dissolution of metallic Co led to the slight increase of the potential difference in the 3rd cycle. The dissolution of metallic Co during cycling will be further discussed in the next section.

The voltage profiles of CoF_2/MWCNTs are shown in Fig. 5b. The first wide voltage plateau at 0.2C appeared above 1.3 V with a discharge capacity of 799 mA h g^{-1}, which is higher than the theoretical capacity of CoF_2 (553 mA h g^{-1}). The extra capacity can be attributed primarily to the interfacial Li storage within the Co/LiF matrix.[24] The charging (delithiation) capacity in the first cycle, that is, the reversible capacity, was 554 mA h g^{-1} at a cutoff voltage of 4.0 V. The sloping voltage curves after the initial lithiation are comparable to the broad peaks of CoF_2/MWCNTs in the CV curves. Conversely, bare-CoF_2 exhibited much lower discharge and charge capacities of 612 and 338 mA h g^{-1}, respectively, in the first cycle (Fig. 5b). The polarization between the discharge and charge voltages of bare-CoF_2 also increased (Fig. 5b and S4†). In addition, the discharge capacity of bare-CoF_2 rapidly decreased to 343 mA h g^{-1} in the second cycle, whereas CoF_2/MWCNTs retained a discharge capacity of 613 mA h g^{-1}. Fig. 5c and d present the rate capabilities of CoF_2/MWCNTs and bare-CoF_2, respectively. CoF_2/MWCNTs exhibited excellent rate performance (Fig. 5c), with a discharge capacity at 2C of 650 mA h g^{-1}. The first charge capacity of CoF_2/MWCNTs at 2C was 469 mA h g^{-1}, which corresponds to a reversible capacity of 84.7% at 0.2C. Table S1† shows the reversible capacity of CoF_2/MWCNTs at 2C in comparison to that of other CoF_2-based cathode materials reported previously,[19,21–23,28,31,35] which demonstrates the superior rate properties of CoF_2/MWCNTs. As CoF_2 nanoparticles were introduced in MWCNTs, ion/electron conduction was facilitated and the reversibility and kinetics of the conversion reaction of CoF_2 improved. However, bare-CoF_2 exhibited an immediate capacity decrease as the C-rate increased, and only 0.3% of the capacity was maintained at 2C compared with the discharge/charge capacity at 0.2C (Fig. 5d).

The overall results indicate that the reversible capacities of CoF_2/MWCNTs were improved, and the rate performance of CoF_2/MWCNTs was considerably enhanced by the addition of MWCNTs and the nanosizing of CoF_2 particles. Nanosized CoF_2 particles and conductive MWCNTs efficiently addressed the intrinsic insulating issue of CoF_2 and the poor kinetics of the conversion reactions. This was further demonstrated by EIS measurements and GITT analysis. Fig. 6a shows the EIS results for CoF_2/MWCNTs and bare-CoF_2. The diameter of the semicircular arc corresponds primarily to the electrochemical charge-transfer resistance (R_{ct}) of the lithium-ion redox reaction at the electrode interface. The small semicircle of CoF_2/MWCNTs indicates improved kinetics of the electrochemical reaction. Electrons are efficiently transferred through the

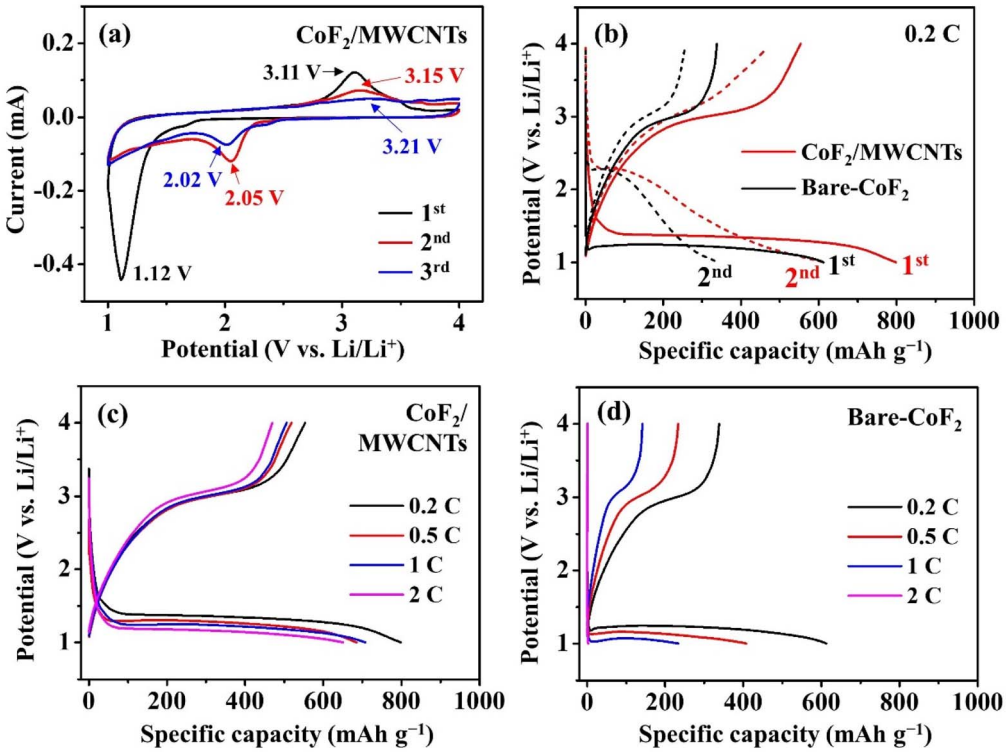

Fig. 5 (a) CV curves of CoF_2/MWCNTs recorded at a scan rate of 0.1 mV s^{-1}. (b) Voltage profiles of CoF_2/MWCNTs and bare-CoF_2 in the 1st and 2nd cycles tested under 0.2C. Voltage profiles of (c) CoF_2/MWCNTs and (d) bare-CoF_2 in the 1st cycle at various C-rates (electrolyte: 1.0 M $LiPF_6$ in EC/DMC).

MWCNTs, and the nanoparticles facilitate the conversion reactions of CoF_2.[23,37] GITT was applied to analyze the overall potential response of CoF_2/MWCNTs and bare-CoF_2 during the first cycle (Fig. 6b). When the current supply was interrupted, the closed-circuit voltage (CCV) during the current pulse changed to quasi-open-circuit-voltage (QOCV) at the end of the relaxation period owing to internal resistance. The internal resistance was calculated by substituting the voltage difference between OCV and QOCV into the equation of Ohm's law (Fig. 6c).[38] The overpotential of CoF_2/MWCNTs was less than that of bare-CoF_2, demonstrating that the conversion reaction kinetics were improved when the small-sized CoF_2 nanoparticles were well-dispersed on the conductive MWCNTs. Note that both CoF_2/MWCNTs and bare-CoF_2 exhibited a decreasing resistance as the CCV was lowered. This trend was likely owing to the formation of conductive Co metal nanoparticles in the composite electrode by the conversion reaction ($CoF_2 + 2Li^+ + 2e^- \rightarrow Co^0 + 2LiF$).[39]

Cycle performance tests were conducted at 0.2C (111 mA g^{-1}). To closely observe the capacities after the first cycle, the discharge capacities were plotted except for the first cycle (Fig. S5a†). Compared with bare-CoF_2, CoF_2/MWCNTs exhibited better cycle performance, maintaining a capacity of 98 mA h g^{-1} over 30 cycles, which is nearly three times higher than that of bare-CoF_2. The discharge capacity increased throughout the cycle owing to the addition of the electroconductive media. Furthermore, the discharge capacity of pure MWCNTs in the 30th cycle was only 19 mA h g^{-1}, considering that the mass ratio of CoF_2 to MWCNTs was 70 : 30 (Fig. S5b†). Thus, MWCNTs serve as conductive materials that facilitate the efficient conversion reaction of CoF_2 in the CoF_2/MWCNT nanocomposites. In particular, the capacity of CoF_2/MWCNTs was attributed primarily to CoF_2. Because the theoretical volume expansion of CoF_2 is not very large (~21 vol%),[20] severe cracks or volumetric changes were not observed on the CoF_2/MWCNT and bare-CoF_2 electrodes (Fig. S6†). However, because rapid capacity fading occurred owing to Co^{2+} dissolution into the electrolyte during cycling,[16] further research to prevent capacity degradation was conducted and will be presented in the next section.

Electrolyte modification for *in situ* formation of the CEI layer

The cycle stability of CoF_2/MWCNTs in different liquid electrolytes was investigated. When an FEC-containing electrolyte was used, the cyclability of CoF_2/MWCNTs increased significantly. As shown in Fig. 7a, CoF_2/MWCNTs with the FEC/EMC electrolyte exhibited a discharge capacity of 241 mA h g^{-1} in the 30th cycle and retained a high capacity of 180 mA h g^{-1} in the 100th cycle. This is approximately 5.5 times higher than the 100th discharge capacity in the EC/DMC electrolytes (33 mA h g^{-1}). These results indicate that the FEC/DMC electrolyte mitigated the capacity degradation of CoF_2/MWCNTs more effectively.

Fig. 7b shows the EIS spectra of the CoF_2/MWCNT cells operated in the FEC/EMC and EC/DMC electrolytes after the 1st cycle. The larger semicircle of the CoF_2/MWCNTs cell operated

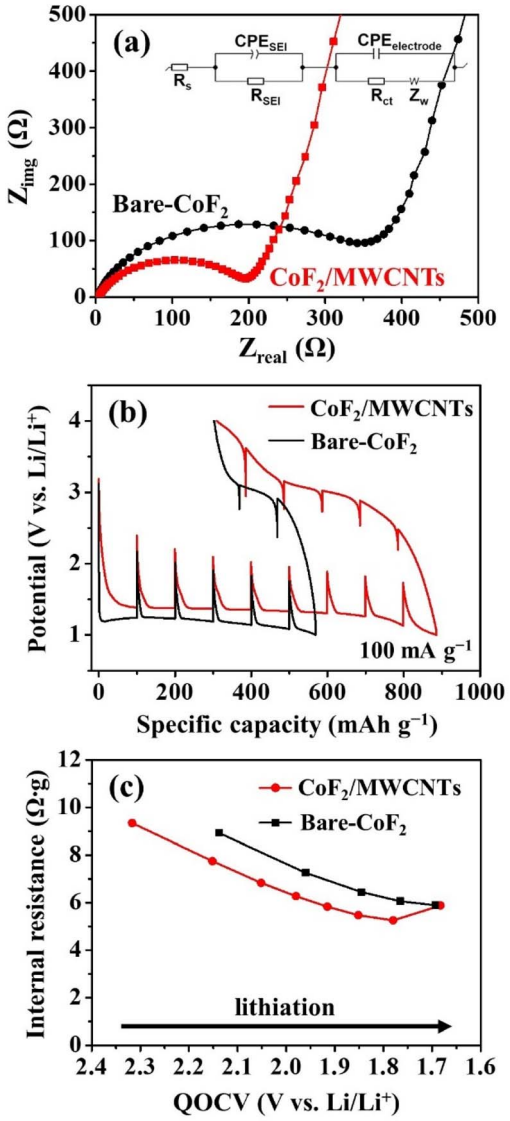

Fig. 6 (a) EIS spectra of CoF_2/MWCNTs and bare-CoF_2 after the 1st cycle (inset: the equivalent circuit model used to fit the EIS data). (b) GITT curves at 100 mA g^{-1} and (c) internal resistance of CoF_2/MWCNTs and bare-CoF_2 (electrolyte: 1.0 M $LiPF_6$ in EC/DMC).

in the FEC/EMC electrolytes indicates a larger resistance of the CoF_2/MWCNT electrode after the 1st cycle. This increase in resistance was primarily due to the *in situ* formation of CEI layers. Compared with Fig. 5c, the voltage profiles in Fig. S7† show that the irreversible discharge capacities of CoF_2/MWCNTs with the FEC/EMC electrolyte increased significantly during the 1st cycle. In particular, the *in situ* formation of numerous CEI layers led to an increase in the irreversible capacity and electrode resistance. Even though the operating voltage was higher than 1.0 V (*vs.* Li/Li^+), solid-electrolyte interphase layers could be formed because the reduction potentials of FEC-containing electrolytes are higher than those of other electrolytes.[23,40–42] Although this reduced the initial discharge/charge efficiency, the sufficiently formed CEI layers mitigated the dissolution of cobalt ions during cycling.

XPS depth profiling of the electrodes after the 1st cycle provided further information on the CEI layers on the electrodes. When using the EC/DMC electrolyte, Co 2p peaks were observed. The peaks at approximately 781.5 and 797.2 eV correspond to the binding energies of Co^{2+} $2p_{3/2}$ and Co^{2+} $2p_{1/2}$, respectively. Considering this result and the voltage profiles of CoF_2/MWCNTs, Co/LiF formed through the discharging process was re-converted to CoF_2 during the charging process and not to other cobalt compounds. Note that the binding energies of Co 2p in Fig. 7c are slightly lower than those of the pristine CoF_2/MWCNTs (Fig. 4a). This phenomenon is presumed to be related to the conditions under which CoF_2 was formed. Previous studies have reported that the binding energy of Co 2p decreases as CoF_2 is synthesized at low temperatures.[43,44] Therefore, compared with the pristine CoF_2/MWCNTs synthesized at 250 °C, the binding energy of CoF_2 formed through the electrochemical conversion reaction at room temperature was lowered. Peaks corresponding to metallic Co were observed as the etching depth increased. The Co 2p peaks at 778.2 and 793.2 eV correspond to Co^0 $2p_{3/2}$ and Co^0 $2p_{1/2}$, respectively. These peaks originate from Co/LiF that did not re-convert to CoF_2 near the core of the particle. By contrast, when the FEC/EMC electrolyte was used, almost no Co 2p peak was observed (Fig. 7c). Even after etching to approximately 10 nm, the intensities of the Co peaks did not increase significantly, indicating the presence of a large number of CEI layers. The appearance of the F 1s peak originated from the components in the CEI layers and not from the Co–F bonding (Fig. 7d). To confirm the stability of the CEI layers, TEM analysis was further conducted using the CoF_2/MWCNT electrodes cycled in the FEC/EMC electrolyte. As shown in Fig. S8,† CEI layers were generated on the surface of CoF_2 particles after the 1st cycle (Fig. S8a†) and stably maintained similar thickness even after the 100th cycle (Fig. S8b–d†).

As mentioned above, such CEI layers improved the cyclability of CoF_2/MWCNTs by mitigating active material dissolution, although it was accompanied by a decrease in the coulombic efficiency and an increase in the interfacial resistance. The post-mortem SEM and EDS analyses of a part of the cycled separators also support this assumption. In the case of the EC/DMC electrolyte cell, severely clogged parts were observed on the surface of the cycled separator (Fig. S9†). The EDS mapping images revealed a high accumulation of cobalt, indicating that the active materials in CoF_2/MWCNTs were significantly dissolved. As the voltage increased during charging, a portion of the metallic cobalt formed during the discharging process could be dissolved as cobalt ions into the electrolyte. The repeated dissolution of cobalt ions during cycling led to the growth of numerous side products and severe degradation of the cells. By sharp contrast, when using the FEC/EMC electrolyte cell, the number of side products on the separator was relatively reduced, and the corresponding EDS mapping showed the partial presence of cobalt (Fig. S10†). Owing to the significant influence of the CEI layers formed by the FEC-containing electrolyte, excessive dissolution of active materials was efficiently mitigated, and the cyclability of CoF_2/MWCNTs could be improved.

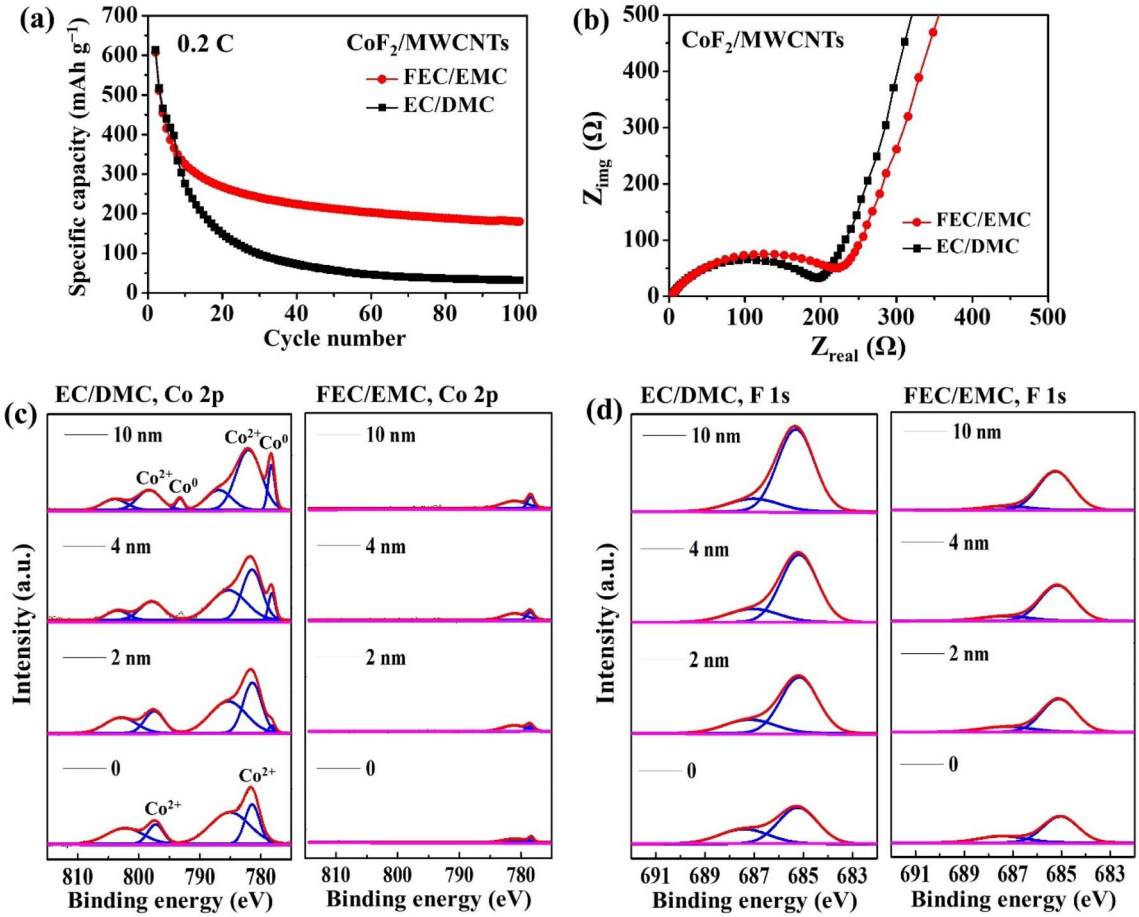

Fig. 7 (a) Cycle performance and (b) EIS spectra after the 1st cycle of CoF_2/MWCNTs with EC/DMC and FEC/EMC electrolytes. In-depth analysis of XPS after the 1st cycle of (c) Co 2p spectra and (d) F 1s spectra with EC/DMC and FEC/EMC electrolytes.

Ex situ Al_2O_3 coating by LAD to reduce capacity fading

Ex situ Al_2O_3 layer coating using ALD was further conducted to reduce undesirable reactions at the interface of the electrode and electrolyte. To explore the effect of the coating thickness, the CoF_2/MWCNT electrodes were coated with Al_2O_3 for 20 or 50 ALD cycles. As shown in Fig. S11a,† the high-resolution TEM image suggests the presence of amorphous Al_2O_3 layers on the CoF_2/MWCNT electrode. Fig. S11b† shows the Al 2p XPS spectra of 20A- and 50A-CoF_2/MWCNTs. The binding energy of 74.5 eV in the XPS spectrum is attributed to the Al–O bond,[45] confirming the existence of Al_2O_3 on the electrode. The peak intensity increased with an increasing number of ALD cycles.

Fig. 8a shows the cycling performance of CoF_2/MWCNTs with different Al_2O_3 coating thicknesses at 0.2C, within a voltage range of 1.0–4.0 V, using the FEC/EMC electrolyte. To closely observe the capacity after the first cycle, the second to 100th cycles were plotted. The discharge capacity of uncoated-CoF_2/MWCNTs continued to decay and exhibited the lowest capacity of 180 mA h g^{-1} in the 100th cycle. In comparison, the discharge capacities of 20A- and 50A-CoF_2/MWCNTs in the 100th cycle were 11% (199 mA h g^{-1}) and 37% (247 mA h g^{-1}) higher than that of the uncoated CoF_2/MWCNTs, respectively. The better cyclability of 50A-CoF_2/MWCNTs indicates that a sufficient Al_2O_3 coating effectively reduced the active material dissolution and improved the electrochemical performance.[19] Interestingly, even though the inactive and non-electrically conductive Al_2O_3 layers are present on 50A-CoF_2/MWCNTs, the results of EIS analysis after the 100th cycle show that 50A-CoF_2/MWCNTs had a lower charge transfer resistance compared to CoF_2/MWCNTs. Therefore, a sufficient Al_2O_3 coating on CoF_2/MWCNTs through ALD suppressed the formation of undesirable resistive species originating from the dissolution of active materials.[46] The long-term cycling stabilities of 20A- and 50A-CoF_2/MWCNTs were further examined. Fig. 8c shows the stable cycling performance of both electrodes over 500 cycles at 0.2C. In particular, 50A-CoF_2/MWCNTs retained a higher capacity of 206 mA h g^{-1} after 500 cycles. The changes in the separator after 500 cycles in the 50A-CoF_2/MWCNT cell were investigated by SEM imaging and EDS mapping (Fig. S12†). Only small amounts of impurities were present on the surface of the separator in the 50A-CoF_2/MWCNT cell with the FEC/EMC electrolyte; a further decrease in side reactions was observed compared with the uncoated-CoF_2/MWCNT cell with the FEC/EMC electrolyte (Fig. S10†). Overall, the results demonstrate that the *ex situ* coating of Al_2O_3 layers is an effective strategy to reduce active material dissolution and

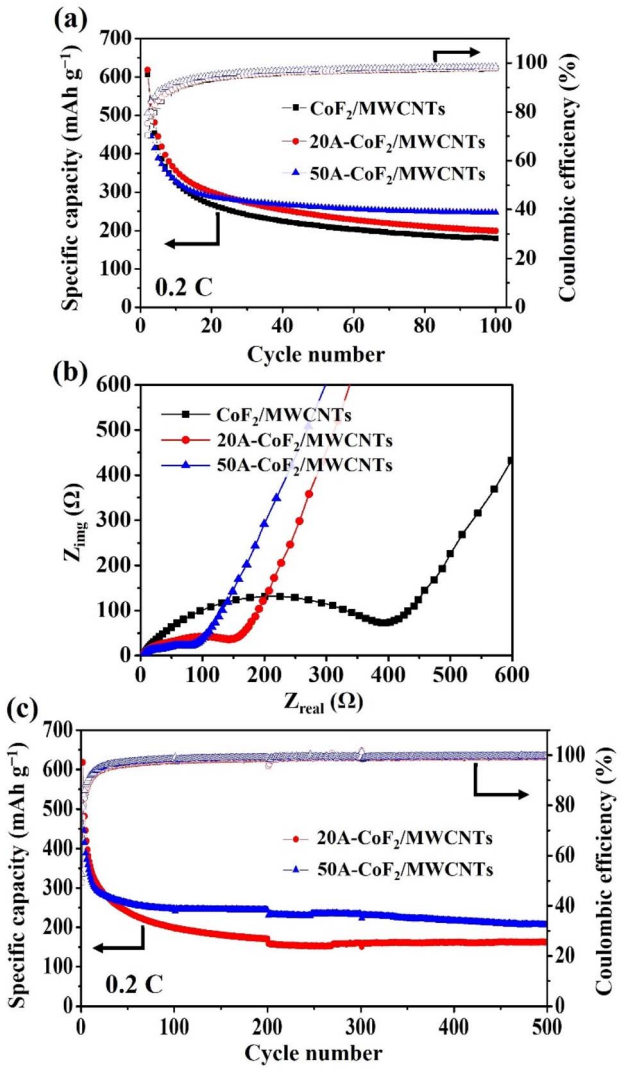

Fig. 8 (a) Cycling performance of CoF_2/MWCNTs, 20A-CoF_2/MWCNTs, and 50A-CoF_2/MWCNTs at 0.2C. (b) EIS spectra of CoF_2/MWCNTs, 20A-CoF_2/MWCNTs, and 50A-CoF_2/MWCNTs after the 100th cycle. (c) Long-term cycle performance of 20A- and 50A-CoF_2/MWCNTs at 0.2C (electrolyte: 1.0 M $LiPF_6$ in FEC/EMC).

improve the long-term cyclability of CoF_2-based cathodes. One thing to note is that the coulombic efficiencies (CEs) of CoF_2/MWCNTs at the early stage of the cycle tests were lower than those of commercial cathode materials for the following reasons. (i) CEI layers formed by the irreversible reduction reactions of the FEC-containing electrolyte. (ii) Some CoF_2 particles that were not closely complexed with MWCNTs exhibited irreversible conversion reactions. (iii) Even though Al_2O_3 and CEI layers existed on the surface of active materials, small amounts of metallic Co became exposed to the electrolyte during the repeated conversion/re-conversion reaction; they could be dissolved in the high voltage region. However, such phenomena mainly occurred at the early stage of the cycle test. Therefore, as the cycle progressed the CEs of CoF_2/MWCNTs increased and they approached approximately 100% at a later stage (Fig. 8a and c).

Conclusions

CoF_2/MWCNTs were synthesized using a facile method developed in this study *via* the precipitation of Co precursors onto MWCNTs, followed by an easy fluorination process with NH_4F. Well-dispersed CoF_2 nanoparticles on electrically conductive MWCNTs facilitated the conversion reaction of CoF_2. As a result, CoF_2/MWCNTs exhibited an improved reversible capacity (554 mA g^{-1} at 0.2C) and excellent rate capability (a capacity retention of 84.7% at 2C *versus* 0.2C) in comparison with bare-CoF_2. In addition, the electrochemical performance of CoF_2/MWCNTs was further improved by *in situ* and *ex situ* surface protection approaches. *In situ* formation of CEI layers using an FEC-containing electrolyte and *ex situ* Al_2O_3 layer coating on the electrode by ALD effectively reduced the dissolution of active materials during cycling. By protecting the active materials from undesirable side reactions with the electrolyte, CoF_2/MWCNTs retained a capacity of more than 200 mA h g^{-1} after 500 cycles. This study proposes a practical material design with advanced synthetic and surface modification methods to improve the electrochemical performance of CoF_2-based cathodes. This study is expected to provide new insights for achieving high-performance LIBs based on new MF_x cathode materials.

Author contributions

H. P. designed and conducted the whole experiments and wrote the manuscript. I.-S. J. and B.-Y. S. carried out material characterization and electrochemical analyses. Y. C. K. supervised this work. S. K. supervised this work and revised the manuscript. J. C. designed this work and contributed to writing the manuscript.

Conflicts of interest

There are no conflicts to declare.

Acknowledgements

This work was supported by the Korea Institute of Energy Technology Evaluation and Planning (KETEP) grant funded by the Korea government (MOTIE) (20219410100120, commercialization technology development of lithium-ion capacitors with sacrificial cathodes for solar ESS). This research was also supported by a National Research Foundation of Korea (NRF) grant funded by the Korea government (RS-2023-00214588).

Notes and references

1 C. Liu, Z. G. Neale and G. Cao, *Mater. Today*, 2016, **19**, 109–123.
2 W. Li, E. M. Erickson and A. Manthiram, *Nat. Energy*, 2020, **5**, 26–34.
3 C.-H. Jung, H. Shim, D. Eum and S.-H. Hong, *J. Korean Ceram. Soc.*, 2021, **58**, 1–27.
4 F. Wu and G. Yushin, *Energy Environ. Sci.*, 2017, **10**, 435–459.

5 K. Turcheniuk, D. Bondarev, V. Singhal and G. Yushin, *Nature*, 2018, **559**, 467–470.
6 L. Wang, Z. Wu, J. Zou, P. Gao, X. Niu, H. Li and L. Chen, *Joule*, 2019, **3**, 2086–2102.
7 K. Turcheniuk, D. Bondarev, G. G. Amatucci and G. Yushin, *Mater. Today*, 2021, **42**, 57–72.
8 R. Saroha, J.-H. Ahn and J. S. Cho, *Korean J. Chem. Eng.*, 2021, **38**, 461–474.
9 Y. Lu, L. Yu and X. W. D. Lou, *Chem*, 2018, **4**, 972–996.
10 R. Prakash, C. Wall, A. K. Mishra, C. Kübel, M. Ghafari, H. Hahn and M. Fichtner, *J. Power Sources*, 2011, **196**, 5936–5944.
11 F. Wu, J. Maier and Y. Yu, *Chem. Soc. Rev.*, 2020, **49**, 1569–1614.
12 C. P. Guntlin, T. Zünd, K. V. Kravchyk, M. Wörle, M. I. Bodnarchuk and M. V. Kovalenko, *J. Mater. Chem. A*, 2017, **5**, 7383–7393.
13 G. G. Amatucci and N. Pereira, *J. Fluorine Chem.*, 2007, **128**, 243–262.
14 F. Klein, B. Jache, A. Bhide and P. Adelhelm, *Phys. Chem. Chem. Phys.*, 2013, **15**, 15876–15887.
15 C. Li, C. Yin, L. Gu, R. E. Dinnebier, X. Mu, P. A. van Aken and J. Maier, *J. Am. Chem. Soc.*, 2013, **135**, 11425–11428.
16 C. Li, C. Yin, X. Mu and J. Maier, *Chem. Mater.*, 2013, **25**, 962–969.
17 Y. Lu, Y. Zhou, Q. Yan and E. Fong, *J. Mater. Chem. A*, 2016, **4**, 2691–2698.
18 Y. Lu, Z.-y. Wen, J. Jin, X.-w. Wu and K. Rui, *Chem. Commun.*, 2014, **50**, 6487–6490.
19 Y. Wang, M. Zhang, Y. Zhang, Y. Wang, W. Liu, C. Yang, V. Kondratiev and F. Wu, *Energy Fuels*, 2022, **36**, 8439–8448.
20 N. Nitta, F. Wu, J. T. Lee and G. Yushin, *Mater. Today*, 2015, **18**, 252–264.
21 X. Wang, W. Gu, J. T. Lee, N. Nitta, J. Benson, A. Magasinski, M. W. Schauer and G. Yushin, *Small*, 2015, **11**, 5164–5173.
22 C. Wall, R. Prakash, C. Kübel, H. Hahn and M. Fichtner, *J. Alloys Compd.*, 2012, **530**, 121–126.
23 F. Wu, V. Srot, S. Chen, M. Zhang, P. A. van Aken, Y. Wang, J. Maier and Y. Yu, *ACS Nano*, 2021, **15**, 1509–1518.
24 J. Tan, L. Liu, S. Guo, H. Hu, Z. Yan, Q. Zhou, Z. Huang, H. Shu, X. Yang and X. Wang, *Electrochim. Acta*, 2015, **168**, 225–233.
25 Y. T. Teng, S. S. Pramana, J. Ding, T. Wu and R. Yazami, *Electrochim. Acta*, 2013, **107**, 301–312.
26 M. J. Armstrong, A. Panneerselvam, C. O'Regan, M. A. Morris and J. D. Holmes, *J. Mater. Chem. A*, 2013, **1**, 10667–10676.
27 Z. Wang, D. Luan, S. Madhavi, Y. Hu and X. W. D. Lou, *Energy Environ. Sci.*, 2012, **5**, 5252–5256.
28 J. Chun, C. Jo, S. Sahgong, M. G. Kim, E. Lim, D. H. Kim, J. Hwang, E. Kang, K. A. Ryu and Y. S. Jung, *ACS Appl. Mater. Interfaces*, 2016, **8**, 35180–35190.
29 W. Choi and A. Manthiram, *J. Electrochem. Soc.*, 2006, **153**, A1760–A1764.
30 D. F. Katowah, S. M. Saleh, S. A. Alqarni, R. Ali, G. I. Mohammed and M. A. Hussein, *Sci. Rep.*, 2021, **11**, 5056.
31 Q. Cheng, Y. Chen, X. Lin, J. Liu, Z. Yuan and Y. Cai, *J. Phys. Chem. C*, 2020, **124**, 8624–8632.
32 J. Rojas, M. Toro-Gonzalez, M. Molina-Higgins and C. Castano, *Mater. Sci. Eng., B*, 2016, **205**, 28–35.
33 R. Sitko, E. Turek, B. Zawisza, E. Malicka, E. Talik, J. Heimann, A. Gagor, B. Feist and R. Wrzalik, *Dalton Trans.*, 2013, **42**, 5682–5689.
34 L. Li, F. Meng and S. Jin, *Nano Lett.*, 2012, **12**, 6030–6037.
35 Q. Zhang, Y. T. Huang, X. Chen, A. Pan, Z. Cai, S. Liu and Y. Zhang, *J. Alloys Compd.*, 2019, **805**, 539–544.
36 C. Li, K. Chen, X. Zhou and J. Maier, *npj Comput. Mater.*, 2018, **4**, 22.
37 A. Nulu, V. Nulu, J. S. Moon and K. Y. Sohn, *Korean J. Chem. Eng.*, 2021, **38**, 1923–1933.
38 J. Oh, E. Lim, J. Chun and C. Jo, *J. Power Sources*, 2022, **521**, 230935.
39 X. Hua, R. Robert, L.-S. Du, K. M. Wiaderek, M. Leskes, K. W. Chapman, P. J. Chupas and C. P. Grey, *J. Phys. Chem. C*, 2014, **118**, 15169–15184.
40 T. Hou, G. Yang, N. N. Rajput, J. Self, S.-W. Park, J. Nanda and K. A. Persson, *Nano Energy*, 2019, **64**, 103881.
41 Q. Huang, T. P. Pollard, X. Ren, D. Kim, A. Magasinski, O. Borodin and G. Yushin, *Small*, 2019, **15**, 1804670.
42 E. Markevich, G. Salitra and D. Aurbach, *ACS Energy Lett.*, 2017, **2**, 1337–1345.
43 Z.-W. Fu, C.-L. Li, W.-Y. Liu, J. Ma, Y. Wang and Q.-Z. Qin, *J. Electrochem. Soc.*, 2004, **152**, E50.
44 M. Li, Y. Gu, Y. Chang, X. Gu, J. Tian, X. Wu and L. Feng, *Chem. Eng. J.*, 2021, **425**, 130686.
45 E. Zhao, O. Borodin, X. Gao, D. Lei, Y. Xiao, X. Ren, W. Fu, A. Magasinski, K. Turcheniuk and G. Yushin, *Adv. Energy Mater.*, 2018, **8**, 1800721.
46 G. Xu, C. Pang, B. Chen, J. Ma, X. Wang, J. Chai, Q. Wang, W. An, X. Zhou and G. Cui, *Adv. Energy Mater.*, 2018, **8**, 1701398.

